Real-space formulation of quantum-mechanical inelastic scattering under complex-valued *n*-fold axially symmetric potentials

2000 J. Phys.: Condens. Matter 12 6693

(http://iopscience.iop.org/0953-8984/12/30/302)

J. Phys.: Condens. Matter **12** (2000) 6693–6707. Printed in the UK PII: S0953-8984(00)11659-5

Real-space formulation of quantum-mechanical inelastic scattering under complex-valued n-fold axially symmetric potentials

A Mayer† and J-P Vigneron

Laboratoire de Physique du Solide, Facultés Universitaires Notre-Dame de la Paix, Rue de Bruxelles 61, B-5000 Namur, Belgium

E-mail: alexandre.mayer@fundp.ac.be

Received 7 February 2000, in final form 26 May 2000

Abstract. A numerical technique is presented which enables the propagation of wave functions in a three-dimensional complex potential-energy distribution, as required for modelling electron 'absorption'. The technique is implemented in a transfer-matrix and Green's-function general procedure to simulate field-emission and electronic projection microscopy. In particular, simulated observations of a small carbon fibre by projection microscopy reveal the effects of absorption on the final images. In the situation considered, absorption is responsible for the reinforcement of the external fringes compared to those located well inside the geometrical projection. In agreement with experimental figures and two-dimensional simulations, it turns out that absorption has to be accounted for to explain the shape of projected images, even if the sample has a low level of opacity.

1. Introduction

Projection microscopes make use of the quasi-radial far propagation of field-emitted [1–9] electrons or ions projected out of small tips. Greatly magnified shadows [10, 11] of an object can be obtained, without any lens, on a distant screen by placing the object at short distances from the tip, inside the beam.

In the Fresnel projection microscope (FPM) [12] the electronic source is a tungsten pyramidal nanoprotrusion, 2 to 3 nm in height, with single-atom sharpness. The object lies on a 3 mm TEM gold grid and the screen is a multiple-channel plate 10 cm distant, coupled to a fluorescent screen. The tip–sample distance is controlled within one ångström precision by using technologies developed for the scanning tunnelling microscope. The field-emission voltage, established between the tip holder and the object-supporting grid, is adjusted in the range of 50–300 V, biases which are low enough to avoid all risks of sample destruction.

Below a critical tip–sample distance, the incoming wave is essentially spherical on the scale of the sample, giving rise to Fresnel diffraction images, still highly correlated with direct-space representation images of the object. The magnifications are typically of the order of 10^5–10^6 and enable the observation of carbon fibres with diameters of a few nanometres. The results depend however on the size of the sample and a given fibre appears 'transparent' or 'opaque' depending on whether its diameter is smaller or larger than 2 nm [13]. This behaviour is attributed to absorption in the fibre, which prevails when the sample thickness exceeds 2 nm.

† Author to whom any correspondence should be addressed.

0953-8984/00/306693+15$30.00

Theoretical support for these electronic projection techniques has been given within the Fresnel–Kirchhoff flat-object formalism [14] and the Green's-function formalism [15,16]. Our approach of the problem is based on both the transfer-matrix and Green's-function formalisms and enables considering the three-dimensional potential-energy distribution between the metallic tip holder and the object-support conducting grid. This allows for simulating the observation of heterogeneous samples by taking account of the strongly varying electric field distribution around the tip and the sample, which is mainly responsible for the position of the virtual projection point [12] and the focusing effect observed with small transparent carbon fibres [17]. Absorption was however not accounted for by our model, since the potential energy was assumed to take exclusively real values, resulting in the conservation of current density.

It is the objective of this paper to extend the theoretical material of references [18–22] for the consideration of potential-energy distributions with complex values. It is shown in section 2 how an imaginary component of the potential energy can describe absorption. In section 3, an extension of the numerical techniques given in references [18, 19] is presented to enable computing the wave-function propagation when the three-dimensional potential-energy distribution takes complex values. As in our previous work, the potential energy is assumed to be n-fold axially symmetric. In section 4, it is shown how to implement these techniques in order to derive solutions with scattering boundary conditions, thus enabling the computation of the total current density associated with all incident states in the metal supporting the field-emission tip. In section 5, the theory is applied to simulate the observation of a small carbon fibre. The application focuses on the effects of absorption on the shape of the projected image.

2. Absorption by complex-valued potentials

To see how adding a negative imaginary component to the potential energy can describe absorption, let us consider the following one-dimensional Schrödinger equation:

$$\left[-\frac{\hbar^2}{2m}\frac{\mathrm{d}^2}{\mathrm{d}z^2} + (V_r - \mathrm{i}V_i)\right]\Psi(z,t) = \mathrm{i}\hbar\frac{\partial}{\partial t}\Psi(z,t) \tag{1}$$

where the positive numbers V_r and V_i are the magnitudes of the real and imaginary components of a homogeneous potential-energy distribution.

Solving this equation by taking $E - \mathrm{i}V_i$ as separation constant leads to the following general solution:

$$\Psi(z,t) = (A\mathrm{e}^{\mathrm{i}(kz-(E/\hbar)t)} + B\mathrm{e}^{\mathrm{i}(-kz-(E/\hbar)t)})\mathrm{e}^{-(V_i/\hbar)t} \tag{2}$$

with

$$k = \sqrt{\frac{2m}{\hbar^2}(E - V_r)}.$$

The corresponding particle probability density decreases over time according to

$$|\Psi(z,t)|^2 \sim \mathrm{e}^{-t/\tau} \tag{3}$$

where the characteristic absorption time τ is given by $\tau = \hbar/(2V_i)$.

Solving equation (1) by taking E as separation constant leads to the next general solution:

$$\Psi(z,t) = A\mathrm{e}^{\mathrm{i}(k_r z-(E/\hbar)t)-k_i z} + B\mathrm{e}^{\mathrm{i}(-k_r z-(E/\hbar)t)+k_i z} \tag{4}$$

with

$$\overline{k} = k_r + \mathrm{i}k_i = \sqrt{\frac{2m}{\hbar^2}[(E - V_r) + \mathrm{i}V_i]}.$$

The two parts of the solution describe travelling waves whose associated particle probability density decreases in space according to

$$|\Psi(z,t)|^2 \sim \mathrm{e}^{-|z|/\lambda} \tag{5}$$

where the characteristic absorption length λ is given by $\lambda = 1/(2k_i)$.

Simple arithmetic shows that

$$\lambda \sim \frac{\hbar^2}{2m}\frac{\sqrt{(2m/\hbar^2)(E-V_r)}}{V_i} = \tau(\hbar k/m) \tag{6}$$

where $\hbar k/m$ is the particle group velocity. In the next section of this paper, we will apply the second method for solving the Schrödinger equation since it is the only alternative for considering a potential-energy distribution whose imaginary component is not constant in space.

The physical origin of this complex potential energy can be found in reference [23]. Considering only inter-electron interactions, complex potentials come basically from the projection of the many-body wave function, through the Hamiltonian term representative of these interactions, on the particular state where the travelling electron has a given energy value E. Absorption has to be understood as the result of coupling with other many-body states where the travelling electron has transferred a part of its energy to the electrons of the material, the total number of electrons and the total energy E_{tot} corresponding to this set of electrons being preserved. It is therefore representative of a transition between two states of the many-body wave function. To treat these transitions rigorously, all states associated with given energy values E of the travelling electron should be considered simultaneously, thus letting the 'absorbed' travelling electrons appear in states associated with lower energy values. It is our opinion however that these electrons can no longer participate in a diffraction pattern, due to the fact that coherence with the travelling electrons originally associated with these lower energy values is lost during the transition. We will therefore consider absorption by adding a negative imaginary component to the potential energy and disregarding coupling between states associated with different values for the energy E of the travelling electron.

3. The Schrödinger equation for n-fold symmetric complex-valued potentials

3.1. Objective

Let us consider the virtual instrument depicted in figure 1. Electrons are provided by a semi-infinite 'Sommerfeld' metal at $z \leqslant 0$ (region I), emitted through a very narrow tip and scattered by a three-dimensional absorbing object in region II, which ends at $z = D$ (typically $D = 10$ nm), and finally projected through a zero-potential region III to be received by a screen at $z = L$ (typically $L = 10$ cm).

In order to compute the total current density on the screen, which results from all incident electronic states in the metal, we need to propagate the wave function through the intermediate region II by considering the relevant three-dimensional complex-valued potential-energy distribution. It is the objective of this section to develop a numerical technique to deal with this propagation. Section 4 will present the way in which it can be implemented in order to derive solutions with appropriate boundary conditions, as required for the simulation of projection microscopy.

3.2. Wave-function expansion

In order to take advantage of situations where the z-axis corresponds to an n-fold symmetry, the scattering problem is formulated in cylindrical coordinates, by using the polar coordinates ϕ

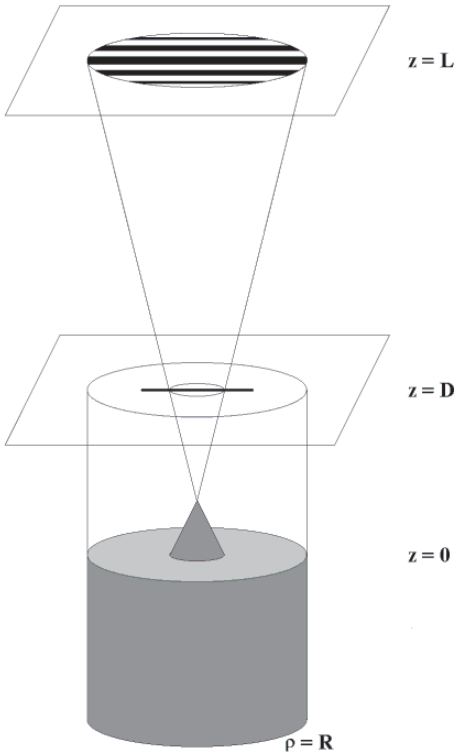

Figure 1. The virtual projection microscope. Electrons are emitted from a small tip, that stands on the flat surface ($z = 0$) of a Sommerfeld metal. After a multiple-scattering process below the sample-supporting grid ($z = D$), the electrons propagate freely to an imaging screen ($z = L$), where a projected image of the sample is obtained. In the region below the sample support ($z \leqslant D$), the electrons are confined in a cylinder with radius R.

(azimuthal angle) and ρ (radial distance to the axis) in the plane normal to the z-axis. Following reference [24], the scattering electrons are assumed to remain localized inside a cylinder with radius R in regions I and II. The following expression can then be used to expand the wave function in these two regions:

$$\Psi(\boldsymbol{r}) = \sum_{m,j} \Phi_{(m,j)}(z)\psi_{(m,j)}(\rho, \phi) \tag{7}$$

where

$$\psi_{(m,j)}(\rho, \phi) = J_m(k_{m,j}\rho)\mathrm{e}^{\mathrm{i}m\phi} \Big/ \sqrt{2\pi \int_0^R \rho \left[J_m(k_{m,j}\rho)\right]^2 \, \mathrm{d}\rho}$$

and the wave vectors $k_{m,j}$ are solutions of $J_m(k_{m,j}R) = 0$. The products $\Phi_{(m,j)}(z)\psi_{(m,j)}(\rho, \phi)$ will be referred to as 'states' of the wave function.

3.3. Potential energy

The potential energy in the intermediate region II ($0 \leqslant z \leqslant D$) is written as $V(\boldsymbol{r})$. Considering the n-fold symmetry, it can be expanded in the form

$$V(\rho, \phi, z) = \left[V_{0,r}(z) + \mathrm{i}V_{0,i}(z)\right] + \sum_{q=-\infty}^{+\infty} \overline{V_r}_q(\rho, z)\mathrm{e}^{\mathrm{i}qn\phi} + \mathrm{i} \sum_{q=-\infty}^{+\infty} \overline{V_i}_q(\rho, z)\mathrm{e}^{\mathrm{i}qn\phi} \tag{8}$$

where the terms with the subscripts r and i correspond respectively to the real and imaginary components of $V(\boldsymbol{r})$. The choice of $V_{0,r}(z)$ and $V_{0,i}(z)$ in this expansion is arbitrary.

The coefficients $\overline{V_{rq}}(\rho, z)$ and $\overline{V_{iq}}(\rho, z)$ are computed from

$$\overline{V_{rq}}(\rho, z) = \frac{n}{2\pi} \int_0^{2\pi/n} \left[\operatorname{Re} V(\rho, \phi, z) - V_{0,r}(z)\right] \mathrm{e}^{-\mathrm{i}qn\phi}\, \mathrm{d}\phi \tag{9}$$

$$\overline{V_{iq}}(\rho, z) = \frac{n}{2\pi} \int_0^{2\pi/n} \left[\operatorname{Im} V(\rho, \phi, z) - V_{0,i}(z)\right] \mathrm{e}^{-\mathrm{i}qn\phi}\, \mathrm{d}\phi. \tag{10}$$

Only coefficients with $q \geqslant 0$ need to be stored, since $\overline{V_{r-q}}(\rho, z) = \overline{V_{rq}}^{*}(\rho, z)$ and $\overline{V_{i-q}}(\rho, z) = \overline{V_{iq}}^{*}(\rho, z)$.

The real component of the potential energy can be computed by applying over-relaxation methods [19, 24] (when the object or the tip is described as a continuous medium) or by dipole self-adjustment methods [18] (for a discrete atomistic view of the object or tip structures). In the following, the imaginary component will be determined empirically, in accordance with the experimental electron penetration depth. A negative imaginary value in the fibre will enforce absorption.

3.4. The propagation equation

If we use expression (7) for the wave function in the Schrödinger equation

$$-\frac{\hbar^2}{2m} \nabla^2 \Psi(\boldsymbol{r}) + V(\rho, \phi, z)\Psi(\boldsymbol{r}) = E\Psi(\boldsymbol{r}) \tag{11}$$

and project the result on the basis functions $\psi_{(m,j)}(\rho, \phi)$, the coefficients $\Phi_{(m,j)}(z)$ turn out to satisfy a one-dimensional set of coupled equations:

$$\frac{\mathrm{d}^2\Phi_{(m,j)}(z)}{\mathrm{d}z^2} + \left[\frac{2m}{\hbar^2}E - k_{m,j}^2\right] = \sum_{m'}\sum_{j'} \left[\Omega_{m,j}^{m',j'}(z) + \mathrm{i}\Pi_{m,j}^{m',j'}(z)\right] \Phi_{(m',j')}(z) \tag{12}$$

with

$$\Omega_{m,j}^{m',j'}(z) = \frac{2m}{\hbar^2} \frac{\int_0^R \mathrm{d}\rho\ \rho \int_0^{2\pi} \mathrm{d}\phi\ \operatorname{Re} V(\rho, \phi, z) J_m(k_{m,j}\rho) J_{m'}(k_{m',j'}\rho) \mathrm{e}^{\mathrm{i}(m'-m)\phi}}{2\pi\sqrt{\int_0^R \mathrm{d}\rho\ \rho \left[J_m(k_{m,j}\rho)\right]^2}\sqrt{\int_0^R \mathrm{d}\rho\ \rho \left[J_{m'}(k_{m',j'}\rho)\right]^2}} \tag{13}$$

$$\Pi_{m,j}^{m',j'}(z) = \frac{2m}{\hbar^2} \frac{\int_0^R \mathrm{d}\rho\ \rho \int_0^{2\pi} \mathrm{d}\phi\ \operatorname{Im} V(\rho, \phi, z) J_m(k_{m,j}\rho) J_{m'}(k_{m',j'}\rho) \mathrm{e}^{\mathrm{i}(m'-m)\phi}}{2\pi\sqrt{\int_0^R \mathrm{d}\rho\ \rho \left[J_m(k_{m,j}\rho)\right]^2}\sqrt{\int_0^R \mathrm{d}\rho\ \rho \left[J_{m'}(k_{m',j'}\rho)\right]^2}}. \tag{14}$$

Considering expression (8) for the potential energy and carrying out the angular integration in equations (13) and (14), one obtains

$$\begin{aligned}\Omega_{m,j}^{m',j'}(z) = {} & \frac{2m}{\hbar^2} V_{0,r}(z)\delta_{m,m'}\delta_{j,j'} \\ & + \frac{2m}{\hbar^2} \sum_q \frac{\int_0^R \mathrm{d}\rho\ \rho\, \overline{V_{rq}}(\rho, \phi) J_m(k_{m,j}\rho) J_{m'}(k_{m',j'}\rho)}{\sqrt{\int_0^R \mathrm{d}\rho\ \rho \left[J_m(k_{m,j}\rho)\right]^2}\sqrt{\int_0^R \mathrm{d}\rho\ \rho \left[J_{m'}(k_{m',j'}\rho)\right]^2}} \delta_{m,qn+m'}\end{aligned} \tag{15}$$

$$\begin{aligned}\Pi_{m,j}^{m',j'}(z) = {} & \frac{2m}{\hbar^2} V_{0,i}(z)\delta_{m,m'}\delta_{j,j'} \\ & + \frac{2m}{\hbar^2} \sum_q \frac{\int_0^R \mathrm{d}\rho\ \rho\, \overline{V_{iq}}(\rho, \phi) J_m(k_{m,j}\rho) J_{m'}(k_{m',j'}\rho)}{\sqrt{\int_0^R \mathrm{d}\rho\ \rho \left[J_m(k_{m,j}\rho)\right]^2}\sqrt{\int_0^R \mathrm{d}\rho\ \rho \left[J_{m'}(k_{m',j'}\rho)\right]^2}} \delta_{m,qn+m'}\end{aligned} \tag{16}$$

so equation (12) becomes

$$\frac{\mathrm{d}^2\Phi_{(m,j)}(z)}{\mathrm{d}z^2} + \left\{\frac{2m}{\hbar^2}E - k_{m,j}^2 - \frac{2m}{\hbar^2}\left[V_{0,r}(z) + \mathrm{i}V_{0,i}(z)\right]\right\}\Phi_{(m,j)}(z) = \sum_q \sum_{j'}\left[M_{m,j}^{q,j'}(z) + \mathrm{i}N_{m,j}^{q,j'}(z)\right]\Phi_{(m-qn,j')}(z) \tag{17}$$

with

$$M_{m,j}^{q,j'}(z) = \frac{2m}{\hbar^2}\frac{\int_0^R \mathrm{d}\rho\ \rho\overline{V_{rq}}(\rho,z)J_m(k_{m,j}\rho)J_{m-qn}(k_{m-qn,j'}\rho)}{\sqrt{\int_0^R \mathrm{d}\rho\ \rho\left[J_m(k_{m,j}\rho)\right]^2}\sqrt{\int_0^R \mathrm{d}\rho\ \rho\left[J_{m-qn}(k_{m-qn,j'}\rho)\right]^2}} \tag{18}$$

$$N_{m,j}^{q,j'}(z) = \frac{2m}{\hbar^2}\frac{\int_0^R \mathrm{d}\rho\ \rho\overline{V_{iq}}(\rho,z)J_m(k_{m,j}\rho)J_{m-qn}(k_{m-qn,j'}\rho)}{\sqrt{\int_0^R \mathrm{d}\rho\ \rho\left[J_m(k_{m,j}\rho)\right]^2}\sqrt{\int_0^R \mathrm{d}\rho\ \rho\left[J_{m-qn}(k_{m-qn,j'}\rho)\right]^2}}. \tag{19}$$

The advantage of exploiting the n-fold symmetry lies in the fact that coupling between different components of the wave function occurs only when the corresponding m-subscripts are separated by a multiple of the symmetry axis order n. There are therefore n independent groups of coupled components, that can be treated separately (see reference [25] for a justification for this assertion from group theory). The numerical difficulties encountered in the computation of the coupling coefficients $M_{m,j}^{q,j'}(z)$ and $N_{m,j}^{q,j'}(z)$ can be drastically reduced by assuming the potential energy to vary in steps in the ρ-direction.

3.5. Numerical implementation

Equation (17) can be processed by assuming the complex-valued potential energy $V(\boldsymbol{r})$ to vary discontinuously along z and take constant values over single steps Δz. Accordingly, we write $V_{0,r}(\Delta z)$, $V_{0,i}(\Delta z)$, $M_{m,j}^{q,j'}(\Delta z)$ and $N_{m,j}^{q,j'}(\Delta z)$ for the first components of the potential energy and the coupling coefficients on a given step Δz.

If the set of coefficients $\Phi_{(m,j)}(z)$ to be dealt with is stored in a vector $\overline{\boldsymbol{\Phi}}(z)$, equation (17) takes the form

$$\frac{\mathrm{d}^2}{\mathrm{d}z^2}\overline{\boldsymbol{\Phi}}(z) + \mathbf{E}\overline{\boldsymbol{\Phi}}(z) = (\mathbf{M} + \mathrm{i}\mathbf{N})\overline{\boldsymbol{\Phi}}(z) \tag{20}$$

where $\mathbf{E}$ is a diagonal matrix which contains the elements

$$\frac{2m}{\hbar^2}E - k_{m,j}^2 - \frac{2m}{\hbar^2}\left[V_{0,r}(\Delta z) + \mathrm{i}V_{0,i}(\Delta z)\right]$$

and $\mathbf{M}$ and $\mathbf{N}$ two matrices containing the coupling coefficients $M_{m,j}^{q,j'}(\Delta z)$ and $N_{m,j}^{q,j'}(\Delta z)$.

Although $\mathbf{E}$, $\mathbf{M}$ and $\mathbf{N}$ are Hermitian, the matrix $\mathbf{G} = \mathbf{E} - \mathbf{M} - \mathrm{i}\mathbf{N}$ has no useful property and must be constructed entirely in each step Δz. Let us store the (computed) complex eigenvalues of $\mathbf{G}$ in the diagonal of a matrix $\boldsymbol{\Lambda}$ and the associated eigenvectors in the columns of a matrix $\mathbf{V}$.

The previous equation becomes

$$\frac{\mathrm{d}^2}{\mathrm{d}z^2}\overline{\boldsymbol{\Phi}}(z) + \mathbf{V}\boldsymbol{\Lambda}\mathbf{V}^{-1}\overline{\boldsymbol{\Phi}}(z) = 0 \tag{21}$$

where $\mathbf{V}^{-1}$ is the inverse of $\mathbf{V}$.

Let us define $\overline{\boldsymbol{\xi}}(z) = \mathbf{V}^{-1}\overline{\boldsymbol{\Phi}}(z)$. Since $\mathbf{G}$ does not depend on z on the step Δz, equation (21) becomes

$$\frac{\mathrm{d}^2}{\mathrm{d}z^2}\overline{\boldsymbol{\xi}}(z) + \boldsymbol{\Lambda}\overline{\boldsymbol{\xi}}(z) = 0. \tag{22}$$

This system of uncoupled equations is easily solved and allows for an analytical propagation of $\overline{\boldsymbol{\xi}}(z)$ over Δz. $\overline{\boldsymbol{\Phi}}(z)$ is retrieved from $\overline{\boldsymbol{\Phi}}(z) = \mathbf{V}\overline{\boldsymbol{\xi}}(z)$.

When the potential energy is real, $\mathbf{V}$ is a unitary matrix and can be inverted by taking its transpose complex conjugate (see references [18, 19]). In the general case where the potential energy is complex, $\mathbf{V}^{-1}$ must be computed numerically. It turns out that standard inversion methods do not enable an efficient propagation. Actually, the accuracy of the phase in the propagated solution is crucial for its decomposition into incident and reflected states (see section 4). This accuracy is however not reached when $\mathbf{V}$ is inverted directly. The solution to this problem consists in inverting $\mathbf{V}$ by using

$$\mathbf{V}^{-1} = (\mathbf{V}^{\dagger}\mathbf{V})^{-1}\mathbf{V}^{\dagger} \tag{23}$$

where the dagger stands for the transpose complex conjugate operation. In this expression, $(\mathbf{V}^{\dagger}\mathbf{V})$ is a positive-definite Hermitian matrix and can be inverted by standard methods. This procedure turns out to be more efficient, since phases are treated exactly by the factor $\mathbf{V}^{\dagger}$, while errors in the factor $(\mathbf{V}^{\dagger}\mathbf{V})^{-1}$ affect essentially the amplitude of the solutions and have a reduced impact on the method efficiency.

4. Solutions with scattering boundary conditions by means of transfer matrices and Green's functions

4.1. Boundary states inside the tip holder and on the conducting grid

The semi-infinite Sommerfeld metal in region I ($z \leqslant 0$) is characterized by measured values of W (the work function) and E_F (the Fermi energy). Since the potential energy in region III ($z \geqslant D$) is set conventionally to the constant value 0 and if V refers to the electric bias established between region I and the conducting grid at $z = D$, the potential energy in region I is given by $V_{met} = eV - W - E_F$ (see again figure 1 for an illustration of the geometry).

Considering these constant potential-energy values, the states of the wave-function expansion (7) in region I and at $z = D$ are given by

$$\Psi^{I,\pm}_{(m,j)}(\boldsymbol{r}) = \mathrm{e}^{\pm \mathrm{i}\sqrt{(2m/\hbar^2)(E-V_{met})-k^2_{m,j}}z}\psi_{(m,j)}(\rho,\phi) \tag{24}$$

for $z \leqslant 0$ and

$$\Psi^{D,\pm}_{(m,j)}(\boldsymbol{r}) = \mathrm{e}^{\pm \mathrm{i}\sqrt{(2m/\hbar^2)E-k^2_{m,j}}z}\psi_{(m,j)}(\rho,\phi) \tag{25}$$

for $z = D$, where the roots are positive reals or complex numbers with positive imaginary parts.

4.2. Local scattering described by transfer matrices in the tip–object region

By using the techniques given in the previous section, each outgoing state $\Psi^{D,+}_{(m,j)}$ can be considered individually and propagated backwards from $z = D$ to $z = 0$, where the corresponding wave function is expanded in terms of incident and reflected basis states. The following set of solutions results from these operations:

$$\overline{\Psi}^{+}_{(m,j)} \overset{z\leqslant 0}{=} \sum_{m',j'} A_{(m',j'),(m,j)}\Psi^{I,+}_{(m',j')} + \sum_{m',j'} B_{(m',j'),(m,j)}\Psi^{I,-}_{(m',j')} \overset{z=D}{=} \Psi^{D,+}_{(m,j)}. \tag{26}$$

Due to the linearity of the Schrödinger equation, these solutions can be combined to derive a set of solutions corresponding to a single incident state $\Psi^{I,+}_{(m,j)}$ in region I:

$$\Psi^{+}_{(m,j)} \overset{z\leqslant 0}{=} \Psi^{I,+}_{(m,j)} + \sum_{m',j'} t^{-+}_{(m',j'),(m,j)}\Psi^{I,-}_{(m',j')} \overset{z=D}{=} \sum_{m',j'} t^{++}_{(m',j'),(m,j)}\Psi^{D,+}_{(m',j')} \tag{27}$$

where the relevant transfer matrices $\mathbf{t}^{++}$ and $\mathbf{t}^{-+}$ result from $\mathbf{t}^{++} = \mathbf{A}^{-1}$ and $\mathbf{t}^{-+} = \mathbf{B}\mathbf{A}^{-1}$. Two other transfer matrices $\mathbf{t}^{--}$ and $\mathbf{t}^{+-}$ describing solutions corresponding to incident states $\Psi^{D,-}_{(m,j)}$ at $z = D$ are obtained in a similar way.

An efficient technique for controlling the numerical instabilities encountered in the computation of these transfer matrices is presented in reference [20]. A generalization of this formalism to deal with non-square transfer matrices is given in reference [22].

4.3. Propagation from the conducting grid to the screen described by Green's functions

Within the Green's-function formalism, it is possible to propagate the solutions $\Psi^{+}_{(m,j)}$ from the conducting grid $z = D$ to the screen in region III (within the Kirchhoff assumption [26] that we can use the expression obtained by the transfer-matrix method for the wave function and its derivatives in the plane $z = D$).

The detailed derivation of this propagation is presented in reference [21]. The result, which assumes a zero potential energy in region III, is given by

$$\Psi^{+}_{(m,j)}(r,\theta,\phi) \overset{r\gg 0}{=} \frac{\mathrm{e}^{\mathrm{i}k_E r}}{r} \sum_{m',j'} t^{++}_{(m',j'),(m,j)} \sigma(\theta, m', j', E) \mathrm{e}^{\mathrm{i}m'\phi} \tag{28}$$

with $k_E = \sqrt{2mE/\hbar^2}$ and

$$\sigma(\theta, m, j, E) = -\frac{\mathrm{e}^{-\mathrm{i}k_E \cos(\theta) D}}{2} \left(\sqrt{k_E^2 - k_{m,j}^2} + k_E \cos(\theta) \right) \mathrm{i}^{1-m} \frac{\mathrm{e}^{\mathrm{i}\sqrt{k_E^2 - k_{m,j}^2} D}}{\sqrt{2\pi \int_0^{2\pi} \left[J_m(k_{m,j}\rho) \right]^2 \rho \, \mathrm{d}\rho}}$$
$$\times \int_0^R \mathrm{d}\rho \, \rho J_m(k_{m,j}\rho) J_m(k_E \sin(\theta)\rho). \tag{29}$$

4.4. Total current density

Each incoming state in the metallic support gives rise to transmitted states in region III. The only incoming states to consider are those associated with a real value of

$$\sqrt{\frac{2m}{\hbar^2}(E - V_{met}) - k_{m,j}^2}.$$

Considering expression (28) and the transfer matrix $\mathbf{t}^{++}$, it is easy to compute the corresponding current density $\boldsymbol{J}^{+}_{(m,j)}(\boldsymbol{r})$.

Taking account of the absence of correlation between the incoming states in the metal and considering their contribution to the density of states, the current density resulting from all incident states with energy E is obtained from the weighted sum [18, 19]

$$\boldsymbol{J}_E(\boldsymbol{r}) = \frac{m}{(R\hbar\pi)^2} \sum_{m,j} \frac{1}{\sqrt{2m(E - V_{met})/\hbar^2 - k_{m,j}^2}} \boldsymbol{J}^{+}_{(m,j)}(\boldsymbol{r}). \tag{30}$$

In this one-electron model, the basis functions are constructed such that the particle probability density of the corresponding state, when integrated over a given cylindrical section of the metal, provides the same result. Each state can thus be considered as representative of the same number $|A|^2$ of electrons in a unit volume of the metal. For the description to be appropriate, we can multiply each basis function $\psi_{(m,j)}$ by the common factor A, determined by the requirement that the particle probability density, when integrated over all possible states and energies in the metal, provides the correct value:

$$\rho_{met} = \frac{1}{3\pi^2} \left(\frac{2mE_F}{\hbar^2} \right)^{3/2}. \tag{31}$$

The factor A is given by the relation [18, 19]

$$\rho_{met} = |A|^2 \frac{2m}{(R\hbar\pi)^2} \int_0^{E_F} \mathrm{d}E \sum_j \frac{1}{2mE/\hbar^2 - k_{0,j}^2} \left(2\pi \int_0^R \rho \left[J_0(k_{0,j}\rho) \right]^2 \mathrm{d}\rho \right)^{-1}. \tag{32}$$

Finally, the total electric current density is obtained by integrating over the energy continuum in the metal:

$$\boldsymbol{j}(\boldsymbol{r}) = (-e) \int_{V_{met}}^{V_{met}+E_F} \boldsymbol{J}_E(\boldsymbol{r}) \, \mathrm{d}E. \tag{33}$$

5. Simulated observation of an absorbing carbon fibre by projection microscopy

Under appropriate conditions, electronic projection microscopes provide Fresnel diffraction figures strongly correlated with the object diffusion strength distribution. This essential feature can be traced to the spherical shape and coherence of the electronic waves, when incident on the object.

The necessity to use nanotips with monatomic termination in order to obtain well contrasted diffraction fringes has already been demonstrated [27]. The dependence of the beam angular spread on the radius of a circular aperture facing the emitting tip was presented in reference [22]. Also, the ability of the technique to provide Fraunhofer and Fresnel diffraction figures was the subject of reference [28]. The sucking-in effect and the question of the observability of the atomic structure of a sample by projection microscopy were considered in reference [21].

The present application focuses on the effects of absorption on the images obtained with small carbon fibres (i.e. fibres whose thickness does not exceed 2 nm). The occurrence of black projections as the result of absorption in thick fibres is already understood from two-dimensional models [12]. Absorption in thin fibres can however induce effects that are better accounted for by methods that consider the three-dimensional aspect of the sample. Simulating the observation of a carbon fibre with 1.4 nm thickness is the objective of this section. In particular the effects of absorption on the projected images are studied.

To represent the metallic support of the field-emission tip, we consider a Fermi energy value E_F of 19.1 eV and a work function W of 4.5 eV (values for tungsten [29]). The conducting grid is separated from this support by $D = 3.5$ nm and the extraction bias is 25 V. The electron source is represented by a conical tip with 1 nm height. The carbon fibre has a dielectric constant [30] of 16.5 and a work function [30] of 4.82 eV. It is oriented along the x-axis and infinite in this direction. Its section in the y–z plane is a square with 1.4 nm thickness. The potential-energy distribution is computed by over-relaxation [18]. This technique provides a solution of $\boldsymbol{\nabla} \cdot \epsilon \, \boldsymbol{\nabla} V = 0$ on the cylindrical grid that describes region II. The idea is to replace iteratively the potential-energy values in each discretization cell by a weighted average of the value in its surrounding cells, until convergence is achieved. The boundary conditions are the known values of the potential energy on $z = 0$ and $z = D$ and an assumed linear behaviour for large ρ. The contribution of the travelling electron is also taken into account when computing the image contribution. A section of this distribution in a plane perpendicular to the fibre is shown in figure 2. Scattering is computed by considering a cancellation radius R of 3.5 nm and m-values ranging from -20 to $+20$.

The current density on the 10 cm distant screen is illustrated in figure 3. The figure corresponds to a Fresnel diffraction pattern and is correlated with a geometrical projection of the part of the fibre that is encountered by the electronic beam, whose size is limited. The current values are those corresponding to the assumptions of this model. If the objective of a

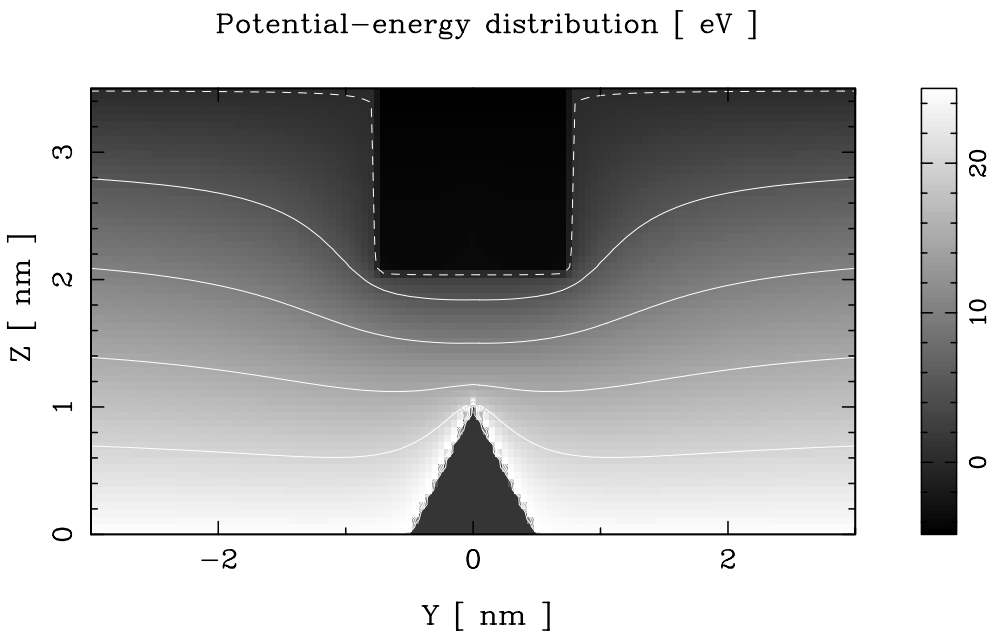

Figure 2. The potential-energy distribution (in eV) in the y–z vertical plane. A 25 V bias is applied over the 3.5 nm separation between the metallic tip-holder surface and the sample-supporting grid. This grid supports a carbon fibre with 1.4 nm thickness that is oriented along the x-axis.

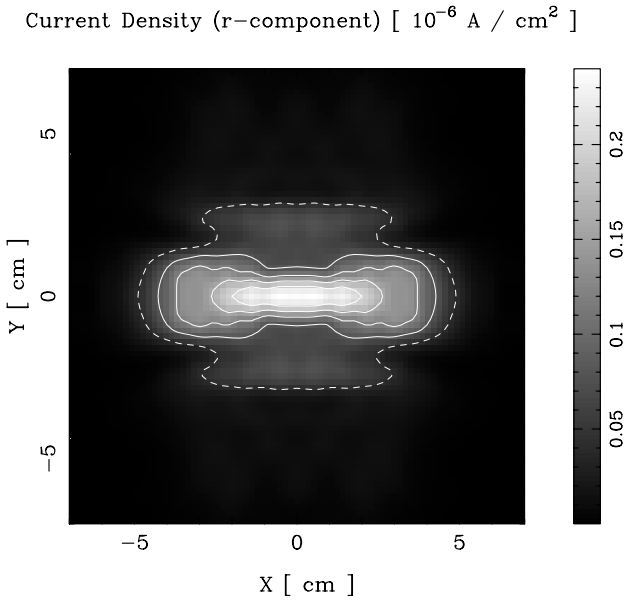

Figure 3. The current density (in A cm^{-2}) on the 10 cm distant screen corresponding to the observation of a carbon fibre with 1.4 nm thickness under a bias of 25 V.

study is the calculation of exact field-emission currents, the modelling of the field-emission structure should be improved.

To see how absorption in the fibre can shape the projected image, its potential energy was given sequentially constant imaginary components of −1 and −4 eV. The −1 eV value

is typically encountered in metals when the energy of the electron is less than 15 eV (see reference [23]). Values around −4 eV are encountered for energies between 15 and 100 eV.

Absorption is expected to be less pronounced in a carbon material than in a metal (where the many free electrons can receive a part of the travelling electron energy). The value of the imaginary part of the potential energy can however be determined in a quantitative way by considering the empirical expression for the inelastic mean free path λ in organic compounds, which (in typical low-energy electron diffraction conditions) is given [31] by

$$\lambda\ (\mathrm{nm}) = \frac{31}{E\ (\mathrm{eV})^2} + 0.087E\ (\mathrm{eV})^{1/2}.$$

From equation (6), V_i is then calculated from

$$V_i = \sqrt{\frac{\hbar^2}{2m}(E - V_r)}\Big/\lambda.$$

With an energy $E = eV - W$ of 20.5 eV and $V_r = -4.82$ eV, we find an imaginary component with an absolute value V_i of 2.1 eV, corresponding to an absorption length λ of 0.47 nm. The physical value $V_i(\boldsymbol{r}) = -V_i$ of the imaginary component of the potential energy in the carbon fibre is hence around the geometrical mean of the two values (−1 and −4 eV) used to study the effect of absorption. The −1 eV value is interesting to consider, since it is responsible in this situation for the electrons being absorbed according to a characteristic length of 1 nm, which agrees with values given in the literature [13]. The −4 eV value is associated with an absorption length around 0.25 nm, enabling the simulated observation of a strongly absorbing material.

Considering a constant imaginary component for the potential energy in the fibre is fully consistent with the approximation of considering a constant real component. The use of these constant values is justified by the limited resolution of the projection technique, which would not be sufficient for the observation of atomic corrugations in the sample. A better description could be achieved by representing the atoms by dipoles [18] or polarized electronic distributions [32] associated with complex polarizabilities.

The current density obtained on the screen when the potential energy in the fibre has an imaginary component of −1 eV is illustrated in figure 4. Absorption is not clearly visible because the equivalent thickness of the sample is a 1.4 characteristic absorption length, so the intensity associated with the electrons travelling through the fibre is only reduced by a factor $e^{1.4} \simeq 4.2$. The projected image remains bright despite absorption and the only significant changes affect the external fringes which tend to be reinforced compared to the central part of the figure.

In figure 5, absorption in the fibre is increased by considering an imaginary component of −4 eV. Since the equivalent thickness of the sample is 5.6 times larger than the characteristic absorption length, the intensity associated with the electrons travelling through the fibre is reduced by a factor $e^{5.6} \simeq 270$. The long-range current density, which results from the part of the beam that does not encounter the fibre, has a reduced (but not entirely cancelled) brightness in the central part of the figure.

A vertical section of the long-range current densities represented in figures 3 to 5 is displayed in figure 6. The central peak is mainly due to electrons travelling through the sample. It is far more affected by absorption than the remaining part of the figure. The intensity of this peak (measured from the top of the curve corresponding to the −4 eV value) is reduced by the factor $e^{1.4} \simeq 4.2$ when $V_i(\boldsymbol{r})$ is increased from 0 to −1 eV in the fibre. The curve corresponding to the −4 eV value is exclusively due to electrons travelling beside the sample. The fact that the main part of the intensity distribution is affected by absorption in

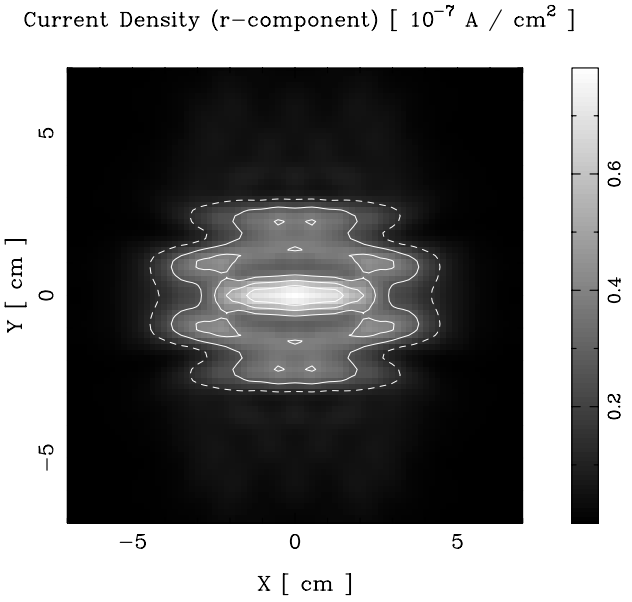

Figure 4. The current density (in A cm^{-2}) on the 10 cm distant screen corresponding to the observation of a carbon fibre with 1.4 nm thickness under a bias of 25 V. The potential energy in the fibre is given an imaginary component of −1 eV.

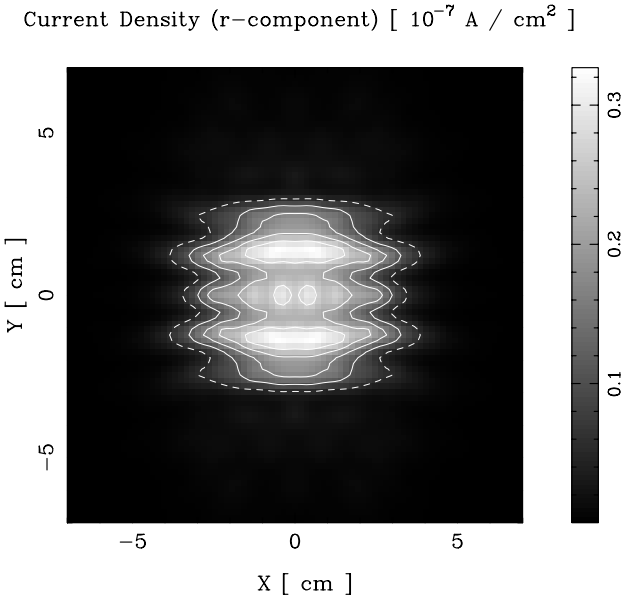

Figure 5. The current density (in A cm^{-2}) on the 10 cm distant screen corresponding to the observation of a carbon fibre with 1.4 nm thickness under a bias of 25 V. The potential energy in the fibre is given an imaginary component of −4 eV.

the fibre is due to the high percentage of the field-emitted electrons being driven through or close to the sample by the surrounding electric field. Comparison of the curve corresponding to the −4 eV value with elementary Fresnel diffraction leads to the conclusion that the virtual projection point is at a distance d of 8 nm from the fibre. This distance enables one to draw the limits (as dotted lines) of a geometrical projection of the sample from this virtual projection point. These limits are those of the central peak associated with electrons travelling through the fibre. The resolution limit due to diffraction of the projection technique is given [12] by $\Delta_d = \frac{1}{2}\sqrt{\lambda d}$ and takes the value of 0.735 nm. Since it is not significantly larger than half of the fibre width (1.4 nm), it confirms the occurrence of Fresnel diffraction.

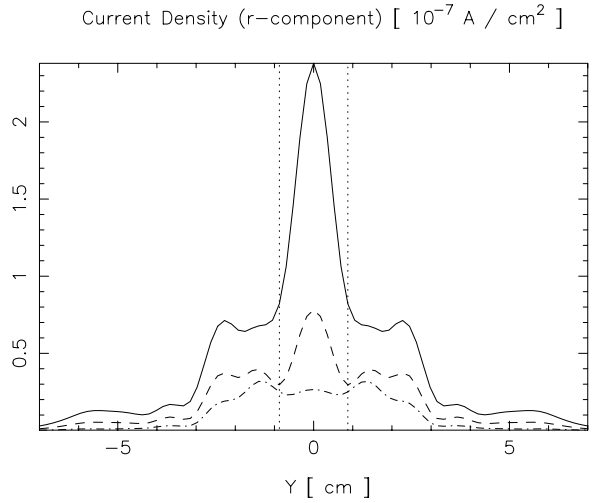

Figure 6. A vertical section of the current density on the 10 cm distant screen corresponding to an imaginary component of the potential energy in the polarizable fibre of 0 eV (continuous), −1 eV (dashed) and −4 eV (dot–dashed). The dotted lines are the limits of the geometrical projection of the fibre, from a 8 nm distant virtual projection point.

For comparison, a vertical section of the long-range current densities obtained when the carbon fibre has a dielectric constant of 1 is represented in figure 7. Since the fibre is not polarized, there is no sucking-in effect of the surrounding electric field. The intensity of the central peak remains however important, compared with the surrounding fringes, due to the very close proximity of the sample to the tip. The increase of absorption in the fibre is again responsible for the reduction of the central peak and the relative increase of the surrounding

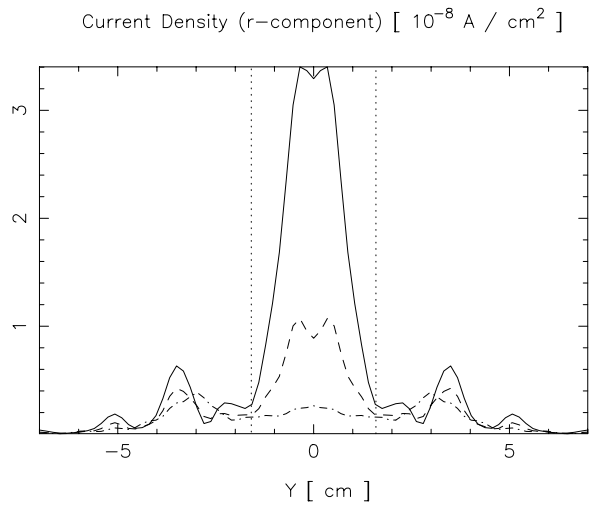

Figure 7. A vertical section of the current density on the 10 cm distant screen corresponding to an imaginary component of the potential energy in the *unpolarizable* fibre of 0 eV (continuous), −1 eV (dashed) and −4 eV (dot–dashed). The dotted lines are the limits of the geometrical projection of the fibre, from a 4.4 nm distant virtual projection point.

fringes. These latter fringes are less affected by absorption than in the previous situation where sucking-in was present. The most striking effect of the lack of surrounding attractive field is the displacement of the virtual projection point from 8 nm to 4.4 nm from the sample. This distance d is again determined by comparison between the curve obtained with $V_i(\boldsymbol{r}) = -4$ eV in the fibre and elementary Fresnel diffraction. The displacement of the virtual projection point due to the converging effect of the electric field surrounding small fibres is observed experimentally [13]. As a consequence of this displacement, the width of the central peak and that of the geometric projection are both increased. The resolution limit due to diffraction Δ_d takes here the value of 0.55 nm, which is smaller than half of the fibre width (1.4 nm), thus explaining the occurrence of Fresnel diffraction.

These bright projected images of thin carbon fibres (in usual conditions where the characteristic absorption length is 1 nm) and the reinforcement of the external fringes are encountered in experiments and in simulations with two-dimensional opaque objects (see reference [12]). This reinforcement of the external fringes, compared to the fringes located inside the geometrical projection of the fibre, can be understood in a Fresnel diffraction regime by relating the external fringes to the part of the beam that does not or hardly encounters the sample. Since this part of the beam does not travel through the fibre, it is not affected by absorption, unlike the other part of the beam which is reduced as absorption becomes more important. When the sample equivalent thickness exceeds several times the characteristic absorption length, only the external part of the beam contributes significantly to the projected image, which becomes dark if appropriate conditions are maintained.

6. Conclusions

Our numerical technique enabling the propagation of wave functions in a three-dimensional potential-energy distribution was extended to include absorption. This technique, implemented in a transfer-matrix and Green's-function general procedure, was applied to simulate the observation of carbon fibres by projection microscopy when absorption is present. In particular, simulations with a small carbon fibre reveal the effects of absorption on the shape of the projected images. In the situation considered, absorption results mainly in a reinforcement of the external diffraction fringes. In agreement with experimental figures and two-dimensional simulations, it turns out that absorption has to be considered to explain the shape of projected images, even if the sample has a low level of opacity.

Acknowledgments

AM was supported as a post-doctoral fellow by the Belgian National Fund for Scientific Research (FNRS). The authors acknowledge the national programme on the Interuniversity Research Project (PAI) and the use of the Namur Scientific Computing Facility, a common project of the FNRS, IBM-Belgium and the FUNDP.

References

[1] Fowler R H and Nordheim L 1928 *Proc. R. Soc.* A **119** 173
[2] Good R H and Müller E 1956 *Handb. Phys.* **21** 176
[3] Burgess R E, Kroemer H and Houston J M 1953 *Phys. Rev.* **90** 515
[4] Young D R 1959 *Phys. Rev.* **113** 110
[5] Stratton R 1964 *Phys. Rev.* **135** 794
[6] Swanson L W and Crouser L C 1967 *Phys. Rev.* **163** 622

[7] He J, Cutler P H, Miskovsky N M, Feuchtwang T E, Sullivan T E and Chung M 1991 *Surf. Sci.* **246** 348
[8] Cutler P H, He J, Miskovsky N M, Sullivan T E and Weiss B 1992 *J. Vac. Sci. Technol.* B **11** 387
[9] Jensen K L and Zaidman E G 1993 *J. Vac. Sci. Technol.* B **12** 776
[10] Melmed A J 1968 *Appl. Phys. Lett.* **12** 100
[11] Fink H-W, Stocker W and Schmid H 1990 *Phys. Rev. Lett.* **65** 1204
[12] Binh V T, Semet V and Garcia N 1995 *Ultramicroscopy* **58** 307
[13] Binh V T and Semet V 1998 *Ultramicroscopy* **73** 107
[14] Binh V T, Semet V, Garcia N and Bitar L 1996 *Optics at the Nanometre Scale* ed M Nieto-Vesperinas and N Garcia (Amsterdam: North-Holland) pp 277–96
[15] Kreuzer H J, Nakamura K, Wierzbicki A, Fink H-W and Schmid H 1992 *Ultramicroscopy* **45** 381
[16] Mayer A, Castiaux A and Vigneron J-P 1998 *Comput. Phys. Commun.* **109** 81
[17] Binh V T and Semet V 1998 *Ultramicroscopy* **73** 107
[18] Mayer A and Vigneron J-P 1997 *Phys. Rev.* B **56** 12 599
[19] Mayer A and Vigneron J-P 1998 *J. Phys.: Condens. Matter* **10** 869
[20] Mayer A and Vigneron J-P 1999 *Phys. Rev.* E **59** 4659
[21] Mayer A and Vigneron J-P 1999 *Phys. Rev.* B **60** 2875
[22] Mayer A and Vigneron J-P 1999 *Phys. Rev.* E submitted
[23] Pendry J B 1974 *Low Energy Electron Diffraction* (New York: Academic)
[24] Laloyaux T, Derycke I, Vigneron J P, Lambin P and Lucas A A 1993 *Phys. Rev.* B **47** 7508
[25] Mayer A and Vigneron J-P 1999 *Phys. Rev.* E **60** 7533
[26] Jackson J D 1962 *Classical Electrodynamics* 2nd edn (New York: Wiley) p 427
[27] Mayer A and Vigneron J-P 1999 *J. Vac. Sci. Technol.* B **17** 506
[28] Mayer A and Vigneron J-P 1999 *Ultramicroscopy* **79** 35
[29] Hagmann M J 1997 *Int. J. Quantum Chem.* **65** 857
[30] Forsythe W E 1954 *Smithsonian Physical Tables* 9th edn (Washington, DC: Smithsonian Institute) pp 427, 635
[31] Seah M and Dench W 1979 *Surf. Interface Anal.* **1** 2
[32] Mayer A, Senet P and Vigneron J-P 1999 *J. Phys.: Condens. Matter* **11** 8617